4 Development of the LDA+DMFT Approach

Alexander Lichtenstein
I. Institut für Theoretische Physik
Universität Hamburg

Contents

1   Introduction

In this lecture, we give an introduction to the theoretical description of strongly correlated materials based on the dynamical mean-field theory (DMFT) and its extensions. The goal of this theoretical construction is to retain the many-body aspects of local atomic physics within the extended solid. The effects of short-range non-local correlations within cluster extensions of the DMFT scheme, as well as long-range fluctuations within the fully renormalized dual-fermion perturbation scheme, are discussed extensively. Recent progress in the numerical solution of the DMFT effective quantum impurity problem within the recently developed continuous-time quantum Monte Carlo schemes is reviewed. We then describe realistic extensions of this approach that combine the accuracy of first-principles density-functional theory (DFT) with the treatment of local many-body effects within DMFT.

Scientific progress in the last century was closely related with the design of silicon based materials for the semiconductor industry. Therefore, the theoretical developments of the last fifty years were associated with realistic electronic structure calculations of such weakly correlated materials. Density-functional theory (DFT) emerged from seminal works of Walter Kohn, Pierre Hohenberg, and Lu Sham [1, 2]. This first-principles scheme is based on an exact theorem, stating that the ground state of interacting electron systems can be found by minimizing a universal functional of the density in some additional external field. The main problem of the DFT scheme is related with the fact that this functional is not known in general and can be calculated numerically with a reasonable accuracy only for the simple case of the homogeneous electron gas. These calculations, which proved to be very useful for the DFT scheme, have been done by David Ceperley and Berni Alder [3] using a two-step quantum Monte Carlo procedure starting from the fixed-node approximation and then releasing the nodal constraint. Nevertheless, the accuracy of such a scheme is still limited and sensitive to the computational details [4]. The main restriction of density-functional theory is that in practice it is restricted to ground state properties, while spectral properties can be found only within the time-dependent DFT scheme [5]. Whereas the structural minimization of complex materials can be carried out very efficiently in the generalized gradient approximation of the DFT, due to the almost spherical properties of the exchange-correlation hole [6], the quality of the spectral properties crucially depends on the systems in question. The TDFT scheme has more problems than the static DFT approach, since there are no suitable time-dependent reference systems to find the exchange-correlation kernel.

Understanding the properties of transition-metal systems is key to important materials like high-temperature superconductors, biological molecules like hemoglobin containing iron, and many others. The enormous progress of the last three decades in designing completely new materials for high-T_c superconductivity, giant and colossal magnetoresistance, or artificially created two-dimensional lattices brings new problems to the theory of transition-metal systems. It turns out that even the ground-state properties of antiferromagnetic oxides or orbitally-ordered compounds are not described well in the DFT scheme [7]. The accurate angle-resolved photoemission study of the cuprate superconductors clearly shows that the spectral properties of such systems with strong electron-electron interactions in the $3d$-shell of transition metals have pro-
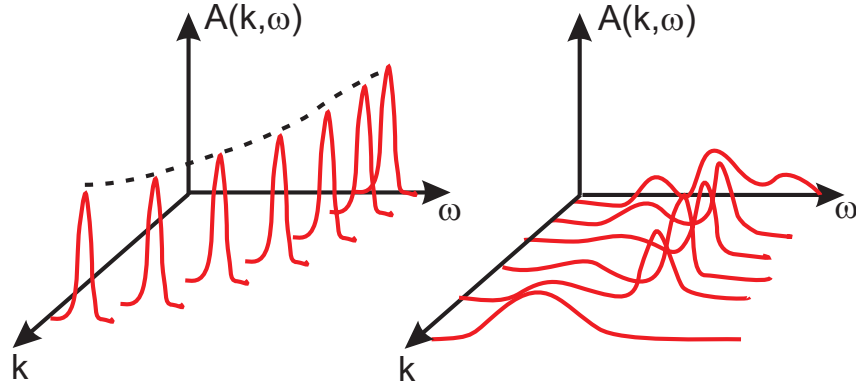
Fig. 1: *Schematic view of ARPES spectra for normal (left) and correlated materials (right).*

nounced incoherent features [8]. We present in Fig. 1 the qualitative difference between the spectral function of normal metals with well defined quasiparticle peaks at all momenta **k** and the strongly correlated case with an incoherent part and a non-quasiparticle spectrum in the Brillouin zone. The main source of the complex correlated behavior of electronic systems, related to strong fluctuations between different low-energy fermionic configurations, is shown schematically in Fig. 2. For example, if the free-energy of electronic systems has only one well defined minimum at zero local moment, then one can expect small electron fluctuations and normal paramagnetic quasiparticle behavior. In the case of two low-lying minima corresponding to singlet and triplet excitations, one can expect strong many body fluctuations and possibly non-quasiparticle behavior related to local Hund's rule physics [9]. In order to treat systems with such effective energy profiles, we need to use the path-integral approach and calculate the corresponding correlation functions using complicated quantum Monte Carlo schemes, which can handle many local minima in the free-energy functional on equal footing.

In this lecture, a general functional approach to the strongly correlated electron systems will be discussed. We will separate the local and non-local correlations and show that it is possible to solve the local correlation problem using the recently developed continuous time Monte Carlo (CT-QMC) scheme. Finally, we discuss an efficient way to go from simple model investigation of strongly correlated systems to realistic investigation of complex electronic materials.
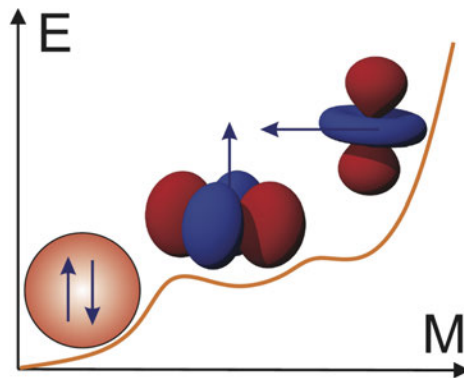
Fig. 2: *Schematic representation of magnetic and orbital fluctuations in correlated systems.*

2   Functional approach: from DFT to DMFT

We introduce a general functional approach which will cover the DFT, Dynamical Mean Field Theory (DMFT) and Baym-Kadanoff (BK) theories [10]. Let us start from the full many–body Hamiltonian describing electrons moving in a periodic external potential of ions $V(\mathbf{r})$ with chemical potential μ and interacting via the Coulomb law: $U(\mathbf{r} - \mathbf{r}') = 1/|\mathbf{r} - \mathbf{r}'|$. We use atomic units $\hbar = m = e = 1$. In the field-operator representation the Hamiltonian has the following form:

$$H = \sum_\sigma \int d\mathbf{r} \hat{\psi}_\sigma^\dagger(\mathbf{r})[-\frac{1}{2}\bigtriangledown^2 + V(\mathbf{r}) - \mu]\hat{\psi}_\sigma(\mathbf{r}) \tag{1}$$

$$+\frac{1}{2}\sum_{\sigma\sigma'} \int d\mathbf{r} \int d\mathbf{r}' \hat{\psi}_\sigma^\dagger(\mathbf{r})\hat{\psi}_{\sigma'}^\dagger(\mathbf{r}')U(\mathbf{r} - \mathbf{r}')\hat{\psi}_{\sigma'}(\mathbf{r}')\hat{\psi}_\sigma(\mathbf{r}).$$

We can always use a single-particle orthonormal basis set $\phi_n(\mathbf{r})$, for example Wannier orbitals, with a full set of quantum numbers, e.g. site, orbital and spin index: $n = (i, m, \sigma)$ and expand the fields in creation and annihilation operators

$$\hat{\psi}(\mathbf{r}) = \sum_n \phi_n(\mathbf{r})\widehat{c}_n \tag{2}$$

$$\hat{\psi}^+(\mathbf{r}) = \sum_n \phi_n^*(\mathbf{r})\widehat{c}_n^+$$

Going from fermionic operators to the Grassmann variables $\{c_n^*,\, c_n\}$, we can write the functional integral representation for the partition function of the many-body Hamiltonian in the imaginary time domain using the Euclidean action S

$$Z = \int \mathcal{D}[c^*, c]e^{-S} \tag{3}$$

$$S = \sum_{12} c_1^*(\partial_\tau + t_{12})c_2 + \frac{1}{2}\sum_{1234} c_1^* c_2^* U_{1234} c_4 c_3, \tag{4}$$

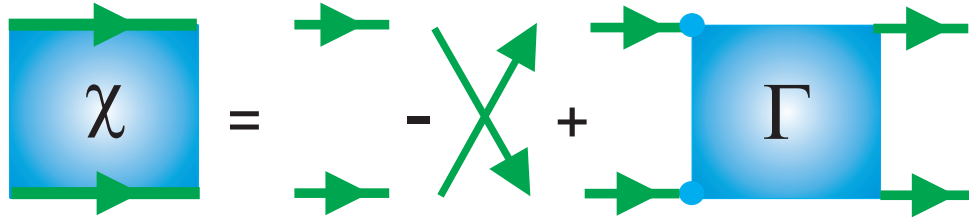where the one- and two-electron matrix elements are defined as following:

$$t_{12} = \int d\mathbf{r}\phi_1^*(\mathbf{r})[-\frac{1}{2}\bigtriangledown^2 + V(\mathbf{r}) - \mu]\phi_2(\mathbf{r}) \tag{5}$$

$$U_{1234} = \int d\mathbf{r} \int d\mathbf{r}' \phi_1^*(\mathbf{r})\phi_2^*(\mathbf{r}')U(\mathbf{r} - \mathbf{r}')\phi_3(\mathbf{r})\phi_4(\mathbf{r}')$$

and we use the following short definition of the sum

$$\sum_1 ... \equiv \sum_{im} \int d\tau... \tag{6}$$

The one-electron Green function is defined via a simple correlation function for fermions

$$G_{12} = -\langle c_1 c_2^* \rangle_S = -\frac{1}{Z} \int \mathcal{D}[c^*, c]\, c_1 c_2^* \exp(-S) \tag{7}$$

Fig. 3: *Representation of full two-particle Green function in terms trivial products of single-particle Green function and the full vertex function Γ.*

The main problem of strongly interacting electronic systems is related to the fact that the higher-order correlation functions are not separated into a product of lower-order correlation functions. For example, the two-particle Green function or generalized susceptibility (X) is defined in the following form [11]

$$X_{1234} =< c_1 c_2 c_3^* c_4^* >_S = \frac{1}{Z} \int \mathcal{D}[c^*, c] \, c_1 c_2 c_3^* c_4^* \exp(-S), \tag{8}$$

and can be expressed graphically through the Green functions and the full vertex function Γ_{1234} [12] (see Fig (3))

$$X_{1234} = G_{14}G_{23} - G_{13}G_{24} + \sum_{1'2'3'4'} G_{11'}G_{22'}\Gamma_{1'2'3'4'}G_{3'3}G_{4'4} \tag{9}$$

In the case of non-interacting electron systems, the high-order correlations X are reduced to the antisymmetrized product of lower-order correlations G, which would correspond to the first two terms (Hartree- and Fock-like) with the vertex function Γ in Eq. (9) equal to zero. In strongly correlated electron systems, the part with the vertex is dominant and even diverges close to electronic phase transitions.

The Baym–Kadanoff functional [13] gives the one–particle Green function and the total free energy at its stationary point. In order to construct the exact functional of the Green function (Baym–Kadanoff) we modify the action by introducing the source term J in the following form

$$S[J] = S + \sum_{12} c_1^* J_{12} c_2. \tag{10}$$

The partition function Z, or equivalently the free energy of the system F, becomes a functional of the auxiliary source field

$$Z[J] = e^{-F[J]} = \int \mathcal{D}[c^*, c] e^{-S'[J]}. \tag{11}$$

Variation of this source functional gives all correlation functions, for example the Green function

$$G_{12} = \frac{\delta F[J]}{\delta J_{21}}|_{J=0}. \tag{12}$$

If we use the definition of the generalized susceptibility as a second variation of the $F[J]$ functional instead of $Z[J]$, one will get only the connected part of the X-function, which is represented by the last term in Eq. (9).

The Baym–Kadanoff functional can be obtained via Legendre transform from J to G

$$F[G] = F[J] - \text{Tr}(JG), \tag{13}$$

We can use the standard decomposition of the free energy F into the single-particle part and the correlated part

$$F[G] = \text{Tr} \ln G - \text{Tr}(\Sigma G) + \Phi[G], \tag{14}$$

were Σ_{12} is single-particle self-energy and $\Phi[G]$ is the correlated part of the Baym–Kadanoff functional and is equal to the sum of all two-particle irreducible diagrams. In the stationary point, this functional gives the free energy of the system. One can use different Legendre transforms and obtain functionals of the self-energy Σ [14] or complicated functionals of two variables G and Γ [15] or a more simple functional of G and screened Coulomb interactions W [10] useful in the GW theory.

In practice, $\Phi[G]$ is not known for interacting electron systems, which is similar to the problem of the functional in the density-functional theory. Moreover, this general functional approach reduces to the DFT if one uses the only the space- and time-diagonal part of the Green function, which corresponds to the one-electron density

$$n_1 = G_{12}\delta_{12} = \langle c_1^* c_1 \rangle_S, \tag{15}$$

with the Kohn–Sham potential $V_{KS} = V_{ext} + V_H + V_{xc}$ playing the role of the "constrained field" - J. Here, V_{ext} is the external potential, and V_H is the Hartee potential. In principle, the exchange-correlation potential V_{xc} is known only for the homogeneous electron gas; therefore, in all practical applications, one use a so-called local density approximation to DFT. In this case, the DFT functional is defined in the following way:

$$F_{DFT}[n] = T_0[n] + V_{ext}[n] + V_H[n] + V_{xc}[n], \tag{16}$$

where T_0 is the kinetic energy of the non-interacting system. Finally, if we define the total electron density as

$$n(\mathbf{r}) = \sum_i \phi_i^*(\mathbf{r})\phi_i(\mathbf{r}),$$

the local density approximation to the DFT reads

$$T_0[n] + V_{ext}[n] = \sum_i \int d\mathbf{r}\phi_i^*(\mathbf{r})\left[-\frac{1}{2}\nabla^2 + V_{ext}(\mathbf{r}) - \mu\right]\phi_i(\mathbf{r}) \tag{17}$$

$$V_H[n] = \frac{1}{2}\int d\mathbf{r}\, n(\mathbf{r})U(\mathbf{r} - \mathbf{r}')n(\mathbf{r}') \tag{18}$$

$$V_{xc}[n] = \int d\mathbf{r}\, n(\mathbf{r})\varepsilon(n(\mathbf{r})), \tag{19}$$

where $\varepsilon(n)$ is exchange-correlation density for the homogeneous electron gas, which can be calculated within a QMC-scheme [3].

In the DFT scheme, we lose information about the non-equal-time Green function, which gives the single-particle excitation spectrum as well as the **k**-dependence of the spectral function, and restrict ourself only to the ground state energy of the many-electron system. Moreover, we also lose information about all collective excitations in solids, such as plasmons or magnons, which can be obtained from the generalized susceptibility or from the second variation of the free-energy.

One can probably find the Baym–Kadanoff interacting potential $\Phi[G]$ for simple lattice models using the quantum Monte Carlo scheme (QMC). Unfortunately, due to the sign problem in lattice simulations, this numerically exact solution of electronic correlations is not possible. On the other hand, one can obtain the solution of the local interacting quantum problem in a general fermionic bath using the QMC scheme, which has no sign problem if it is diagonal in spin- and orbital-space. Therefore, a reasonable approach to strongly correlated systems is to keep only the local part of the many-body fluctuations. In such a Dynamical Mean-Field Theory (DMFT), one can obtain numerically the correlated part of the local functional. In this scheme, we only use the local part of the many-electron vertex and obtain in a self-consistent way an effective functional of the local Green function. In the following section we discuss the general dual fermion (DF) transformations [16] that help us to separate the local fluctuations in many-body system and shows a perturbative way to go beyond the DMFT approximations.

3 Local correlations: DMFT and beyond

We will only consider the local but multiorbital interaction vertex $U^i_{mm'm''m'''}$. Sometimes we will omit all orbital indices for simplicity. All equations will be written in matrix form, giving an idea of how to generalize a DF scheme to the multiorbital case [17, 18]. The general strategy to separate the local and non-local correlation effects is associated with the introduction of auxiliary fermionic fields that will couple separated local correlated impurities models back to the lattice [16]. In order to include the smaller non-local part of the Coulomb interactions, one can use a more general approach consists of auxiliary fermionic and bosonic fields [19].

We rewrite the corresponding original action from Eq. (3) in Matsubara space as a sum of the non-local one-electron contribution with t_{12} and the local interaction part U:

$$S[c^*, c] = - \sum_{\omega \mathbf{k} \sigma \, mm'} c^*_{\omega \mathbf{k} \sigma m} \left[(i\omega + \mu)\mathbf{1} - t^{mm'}_{\mathbf{k}\sigma} \right] c_{\omega \mathbf{k} \sigma m'} + \sum_i S_{\mathrm{U}}[c^*_i, c_i]. \tag{20}$$

where $\omega = (2n+1)\pi/\beta, (\Omega = 2n\pi/\beta), n = 0, \pm 1, ...$ are the fermionic (bosonic) Matsubara frequencies, β is the inverse temperature, μ is the chemical potential. The index i labels the lattice sites, m refers to different orbitals, σ is the spin projection, and the **k**-vectors are quasi-momenta. In order to keep the notation simple, it is useful to introduce the combined index $\alpha \equiv \{m, \sigma\}$. Translational invariance is assumed for simplicity in the following, although a real-space formulation is straightforward. The local part of the action S_{U} may contain any type of local multi-orbital interaction.
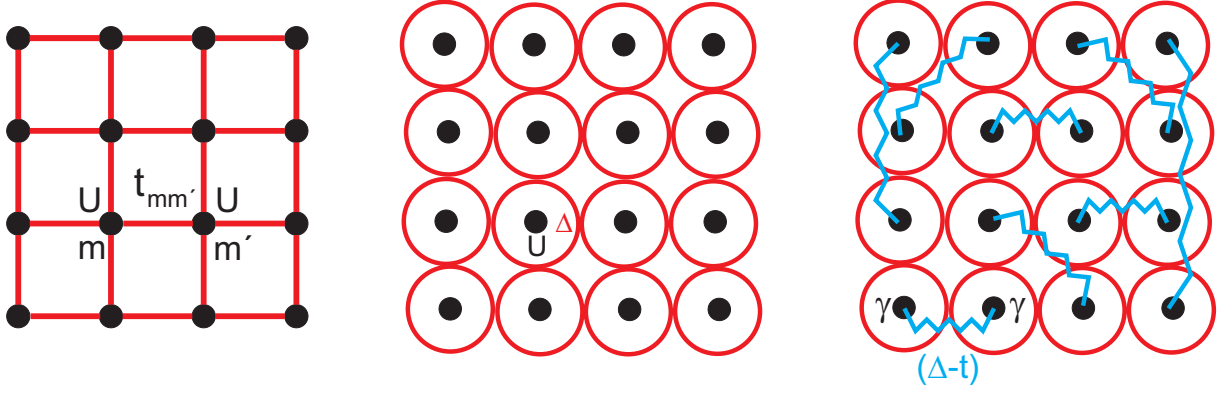
Fig. 4: *From the lattice model (left) to the real-space DMFT (middle) following up with the non-local DF perturbation (right).*

In order to formulate an expansion around the best possible auxiliary local action, a quantum impurity problem is introduced:

$$S_{\mathrm{loc}}[c^*, c] = -\sum_{\omega\,\alpha\beta} c^*_{\omega\alpha} \left[(i\omega + \mu)\mathbf{1} - \Delta^{\alpha\beta}_\omega\right] c_{\omega\beta} + S_{\mathrm{U}}[c^*, c], \tag{21}$$

where Δ_ω is the effective hybridization matrix describing the coupling of the impurity to an auxiliary fermionic bath. The main motivation for rewriting the lattice action in terms of a quantum impurity model is that such a reference system can be solved numerically exactly for an arbitrary hybridization function using the CT-QMC method [20]. Using the locality of the hybridization function Δ_ω, the lattice action (20) can be rewritten exactly in terms of individual impurity models and the effective one-electron coupling $(t_{ij} - \Delta_\omega)$ between different impurities:

$$S[c^*, c] = \sum_i S_{\mathrm{loc}}[c^*_i, c_i] + \sum_{\omega\mathbf{k}\,\alpha\beta} c^*_{\omega\mathbf{k}\alpha} \left(t^{\alpha\beta}_{\mathbf{k}} - \Delta^{\alpha\beta}_\omega\right) c_{\omega\mathbf{k}\beta}. \tag{22}$$

We will find the condition for the optimal choice of the hybridization function later. Although we can solve the individual impurity model exactly, the effect of spatial correlations due to the second term in Eq. (22) is very hard to treat even perturbatively, since the impurity action is non-Gaussian and one cannot use the Wick theorem . The main idea of a dual-fermion transformation is to change variables from (c^*, c) to weakly correlated Grassmann fields (f^*, f) in the path-integral representation for the partition function from Eq. (3), followed by a simple perturbation treatment. The new variables were introduced through the following Hubbard-Stratonovich transformation

$$\exp\left(c^*_\alpha b_\alpha (M^{-1})_{\alpha\beta} b_\beta c_\beta\right) = \frac{1}{\det M} \int \mathcal{D}[f^*, f] \exp\left(-f^*_\alpha M_{\alpha\beta} f_\beta - c^*_\alpha b_\alpha f_\alpha - f^*_\beta b_\beta c_\beta\right). \tag{23}$$

In order to transform the exponential of the bilinear term in (22), we choose the matrices $M_{\alpha\beta}$, and scaling function b_α (if we assume for simplicity that the local Green function is diagonal in orbital and spin space) in accordance with Refs. [16] as

$$M = g_\omega^{-1} \left(\Delta_\omega - t_{\mathbf{k}}\right)^{-1} g_\omega^{-1}, \qquad b = g_\omega^{-1}, \tag{24}$$

where g_ω is the local, interacting Green function of the impurity problem

$$g_{12} = -\langle c_1 c_2^* \rangle_{\rm loc} = -\frac{1}{\mathcal{Z}_{\rm loc}} \int \mathcal{D}[c^*, c] c_1 c_2^* \exp\left(-S_{\rm loc}[c^*, c]\right). \tag{25}$$

With this choice, the lattice action transforms to

$$S[c^*, c, f^*, f] = \sum_i S^i_{\rm site} + \sum_{\omega \mathbf{k} \, \alpha\beta} f^*_{\omega \mathbf{k} \alpha}[g_\omega^{-1} \left(\Delta_\omega - t_\mathbf{k}\right)^{-1} g_\omega^{-1}]_{\alpha\beta} f_{\omega \mathbf{k} \beta}. \tag{26}$$

Hence the coupling between sites is transferred to a local coupling to the auxiliary fermions

$$S^i_{\rm site}[c_i^*, c_i, f_i^*, f_i] = S_{\rm loc}[c_i^*, c_i] + \sum_{\alpha\beta} f^*_{\omega i \alpha} \, g_{\omega \, \alpha\beta}^{-1} c_{\omega i \beta} + c^*_{\omega i \alpha} \, g_{\omega \, \alpha\beta}^{-1} f_{\omega i \beta}. \tag{27}$$

Since g_ω is local, the sum over all states labeled by $\mathbf{k}$ could be replaced by the equivalent summation over all sites by a change of basis in the second term. The crucial point is that the coupling to the auxiliary fermions is purely local and $S_{\rm site}$ decomposes into a sum of local terms. The lattice fermions can therefore be integrated out from $S_{\rm site}$ for each site i separately. This completes the change of variables

$$\int \mathcal{D}[c^*, c] \exp\left(-S_{\rm site}[c_i^*, c_i, f_i^*, f_i]\right) = \mathcal{Z}_{\rm loc} \exp\left(-\sum_{\omega \, \alpha\beta} f^*_{\omega i \alpha} \, g_{\omega \, \alpha\beta}^{-1} f_{\omega i \beta} - V_i[f_i^*, f_i]\right). \tag{28}$$

The above equation may be viewed as the defining equation for the dual potential $V[f^*, f]$. The choice of matrices (24) ensures a particularly simple form of this potential. An explicit expression is found by expanding both sides of Eq. (28) and equating the resulting expressions by order. Formally, this can be done to all orders, and in this sense the transformation to the dual fermions is exact. For most applications, the dual potential is approximated by the first non-trivial interaction vertex

$$V[f^*, f] = \frac{1}{4} \gamma_{1234} f_1^* f_2^* f_4 f_3, \tag{29}$$

where the combined index $1 \equiv \{\omega\alpha\}$ comprises frequency, spin, and orbital degrees of freedom. γ is the exact, fully antisymmetric, reducible two-particle vertex of the local quantum impurity problem. It is given by
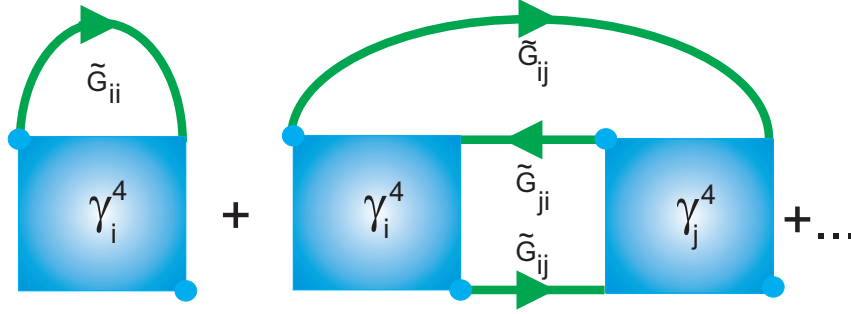
$$\gamma_{1234} = g_{11'}^{-1} g_{22'}^{-1} \left[\chi_{1'2'3'4'} - \chi^0_{1'2'3'4'}\right] g_{3'3}^{-1} g_{4'4}^{-1}, \tag{30}$$

with the two-particle Green function of the impurity being defined as

$$\chi_{1234} = \langle c_1 c_2 c_3^* c_4^* \rangle_{\rm loc} = \frac{1}{\mathcal{Z}_{\rm loc}} \int \mathcal{D}[c^*, c] c_1 c_2 c_3^* c_4^* \exp\left(-S_{\rm loc}[c^*, c]\right). \tag{31}$$

The disconnected part reads

$$\chi^0_{1234} = g_{14} g_{23} - g_{13} g_{24}. \tag{32}$$

Fig. 5: *Diagrams contributing to the dual self-energy $\tilde{\Sigma}$.*

The single- and two-particle Green functions can be calculated using the CT-QMC Monte Carlo algorithms [20]. After integrating out the lattice fermions, the dual action depends on the new variables only and reads

$$\tilde{S}[f^*, f] = -\sum_{\omega \mathbf{k} \, \alpha\beta} f^*_{\omega \mathbf{k} \alpha} [\tilde{G}^0_\omega(\mathbf{k})]^{-1}_{\alpha\beta} f_{\omega \mathbf{k} \beta} + \sum_i V_i[f^*_i, f_i]. \tag{33}$$

and the bare dual Green function is found to be

$$\tilde{G}^0_\omega(\mathbf{k}) = \left[g_\omega^{-1} + \Delta_\omega - t_{\mathbf{k}}\right]^{-1} - g_\omega, \tag{34}$$

which involves the local Green function g_ω of the impurity model.

Up to now, Eqs. (33), (34) are merely a reformulation of the original problem. In practice, approximate solutions are constructed by treating the dual problem perturbatively. Several diagrams that contribute to the dual self-energy are shown in Fig. 5. These are constructed from the impurity vertices and dual Green functions as lines. The first diagram is purely local, while higher orders contain nonlocal contributions, e.g., the second diagram in Fig. 5. In practice, approximations to the self-energy are constructed in terms of skeleton diagrams. The lines shown in Fig. 5 are therefore understood to be fully dressed propagators. The use of skeleton diagrams is necessary to ensure that the resulting theory is conserving in the Baym-Kadanoff sense [13], i.e., that it fulfills the basic conservation laws for energy, momentum, spin, and particle number. The most useful property of such a dual perturbation theory is good convergence both in the weak-coupling limit, when the local vertex is small, and in the strong-coupling limit, when the dual Green function is small [21].

Finally, we can understand the general dual-fermion scheme (Fig. 6) as a two-step process for $\mathbf{k}$-dependent self-energy. First, we need to find an optimal hybridization function Δ_ω, which defines an effective impurity model. Using a numerically exact Monte-Carlo impurity solver, we can obtain the local Green function g_ω which, together with the hopping parameters, defines the non-local dual Green function $\tilde{G}^0_\omega(\mathbf{k})$ and the interaction vertex $\gamma^\Omega_{\omega,\omega'}$, which can be used in renormalized dual perturbation theory [16].

The hybridization function Δ, which so far has not been specified, allows us to optimize the starting point of the perturbation theory and should be chosen in an optimal way. The condition that the first diagram (Fig. 5), as well as all local diagrams with higher order correlation functions in the expansion of the dual self-energy, must be equal to zero at all frequencies fixes the
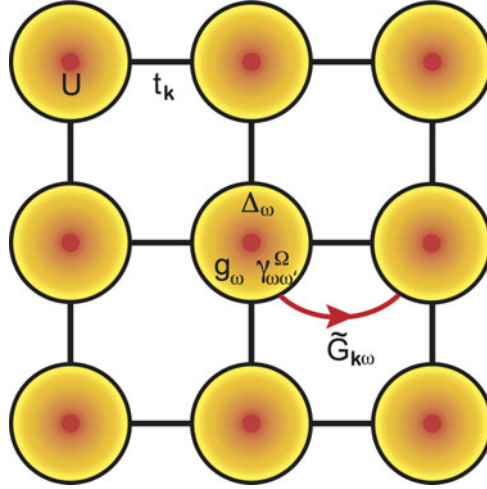
Fig. 6: *General view on dual-fermiom approach: effective impurity model defined by hybridization function Δ_ω. It can be exactly solved within CT-QMC, resulting in single-particle Green function g_ω and full connected vertex $\gamma^\Omega_{\omega,\omega'}$ with two fermionic (ω) and one bosonic (Ω) Matsubara frequencies. Based on this local information, one can perform an efficient lattice perturbation expansion for the dual Green function $\tilde{G}^0_\omega(\mathbf{k})$.*

hybridization. This eliminates the leading-order diagrammatic correction to the self-energy and establishes a connection to DMFT, which can be seen as follows: since the γ vertex is local, this condition amounts to demanding that the local part of the dual Green function be zero:

$$\sum_{\mathbf{k}} \tilde{G}_\omega(\mathbf{k}) = 0. \tag{35}$$

The simplest nontrivial approximation is obtained by taking the leading-order correction, the first diagram in Fig. 5, evaluated with the bare dual propagator (34). Using the expression for the DMFT Green function [22]:

$$G^{\mathrm{DMFT}}_\omega(\mathbf{k}) = \left[g^{-1}_\omega + \Delta_\omega - t_{\mathbf{k}} \right]^{-1}, \tag{36}$$

it immediately follows that (35) evaluated with the bare dual Green function is exactly equivalent to the DMFT self-consistency condition for Δ_ω :

$$\frac{1}{N_{\mathbf{k}}} \sum_{\mathbf{k}} G^{\mathrm{DMFT}}_\omega(\mathbf{k}) = g_\omega. \tag{37}$$

In the limit of infinitely large lattice connectivity, the DMFT scheme becomes exact with local self-energy [23]. The DMFT approximation for real lattice models appears to be one of the most successful many-body schemes for realistic multi-orbital systems [10]. Since it involves the exact solution of the many-body multi-orbital impurity model Eq. (25), all local quantum fluctuations of different orbitals, spins, and charges (Fig. (7)) are included in this scheme.

In the DMFT approach, one can study paramagnetic correlated phases of complex crystals with strong spin and orbital fluctuations above transition temperatures of the spin- and orbital-ordered states [24]. Hence, DMFT appears as the zero-order approximation in this approach,
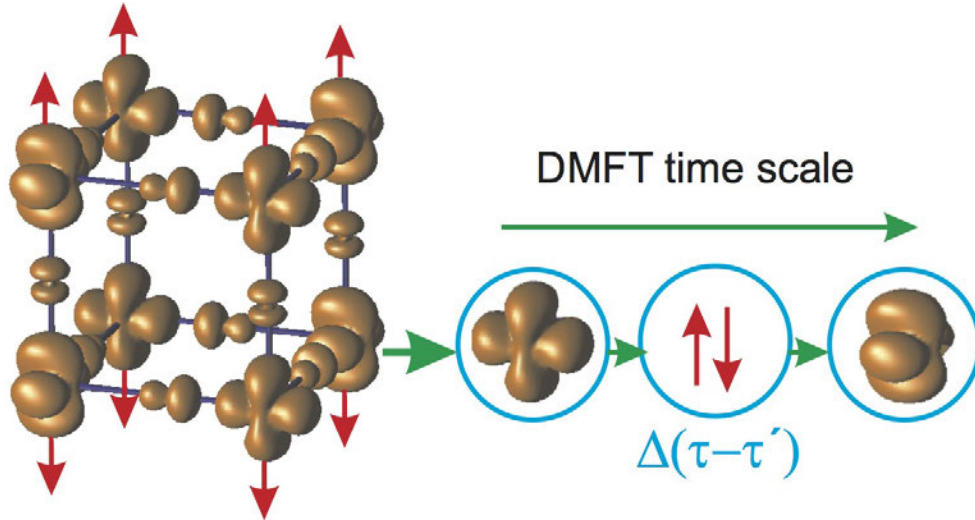
Fig. 7: *Schematic representations of initial lattice model (left) and the local DMFT approach with orbital and spin fluctuations.*

and corrections to DMFT are included perturbatively. A formal relation to DMFT can be established using the Feynman variational functional approach. In this context, DMFT appears as the optimal approximation to a Gaussian ensemble of dual fermions [25].

When diagrammatic corrections are taken into account and the first diagram is evaluated with the dressed propagator $\tilde{G}$, the condition (35) will in general be violated. It can be reinforced by adjusting the hybridization function iteratively. This corresponds to eliminating an infinite partial series of all local diagrams starting from the first term in Fig. 5. These contributions are effectively absorbed into the impurity problem. Note that such an expansion is not around DMFT, but rather around an optimized impurity problem.

The only difference between a DMFT and a DF calculation are the diagrammatic corrections that are included into the dual Green function. To this end, the local impurity vertex γ has to be calculated in addition to the Green function in the impurity solver step.

It is an important consequence of the exact transformation (23) that for a theory that is conserving in terms of dual fermions, the result is also conserving in terms of lattice fermions [25]. This allows the construction of general conserving approximations within the dual fermion approach. Numerically, the self-energy is obtained in terms of skeleton diagrams by performing a self-consistent renormalization as described below. Once an approximate dual self-energy is found, the result may be transformed back to a physical result in terms of lattice fermions using exact relations.

The action (33) allows for a Feynman-type diagrammatic expansion in powers of the dual potential V. The rules are similar to those of the antisymmetrized diagrammatic technique [26]. Extension of these rules to include generic n-particle interaction vertices is straightforward. Due to the use of an antisymmetrized interaction, the diagrams acquire a combinatorial prefactor. For a tuple of n equivalent lines, the expression has to be multiplied by a factor $1/n!$. As the simplest example we can write schematically the first self-energy correction of the diagram

in Fig. 5, which contains a single closed loop

$$\tilde{\Sigma}_{12}^{(1)} = -T \sum_{34} \gamma_{1324} \tilde{G}_{43}^{\mathrm{loc}}, \tag{38}$$

where $\tilde{G}^{\mathrm{loc}} = (1/N_{\mathbf{k}}) \sum_{\mathbf{k}} \tilde{G}(\mathbf{k})$ denotes the local part of the dual Green function. The second-order contribution represented in Fig. 5 contains two equivalent lines and one closed loop and hence is $\mathbf{k}$-dependent

$$\tilde{\Sigma}_{12}^{(2)}(\mathbf{k}) = -\frac{1}{2} \left(\frac{T}{N_k} \right)^2 \sum_{\mathbf{k}_1 \mathbf{k}_2} \sum_{345678} \gamma_{1345} \tilde{G}_{57}(\mathbf{k}_1) \tilde{G}_{83}(\mathbf{k}_2) \tilde{G}_{46}(\mathbf{k} + \mathbf{k}_2 - \mathbf{k}_1) \gamma_{6728} \tag{39}$$

In practice, it is more efficient to evaluate the lowest order diagrams in real space and transform back to reciprocal space using the fast Fourier transform. After calculating the best possible series for the self-energy $\tilde{\Sigma}$ in the dual space, one can calculate the renormalized Green function matrix for original fermions using the following simple transformation [19]

$$G_{\omega}(\mathbf{k}) = \left[\left(g_{\omega} + g_{\omega} \tilde{\Sigma}_{\omega}(\mathbf{k}) g_{\omega} \right)^{-1} + \Delta_{\omega} - t_{\mathbf{k}} \right]^{-1}, \tag{40}$$

which is a useful generalization of the DMFT Green function (see Eq. (36)) to include non-local correlation effects. One can see that the dual self-energy plays the role of of an effective T-matrix for the exactly solvable local problem.

The progress of the DMFT approach is strongly related to developments of efficient numerical solvers for an effective quantum impurity model.

4 Multiorbital quantum impurity solvers

Even though DMFT reduces the extended lattice problem to a single-site problem, the solution of the underlying Anderson impurity model remains a formidable quantum many-body problem that requires accurate solvers. Recently, a new class of solvers has emerged, the continuous-time quantum impurity solvers. These are based on stochastic Monte-Carlo methods and mainly come in two different flavors: The weak- and strong-coupling approach.

The weak-coupling or interaction expansion continuous-time (CT-INT) quantum Monte Carlo algorithm for fermions was originally introduced by Aleksei Rubtsov [27]. There are two main previous attempts: first, work by Nikolay Prokof'ev et $al.$ [29], who devised a continuous-time scheme to sample the infinite series of Feynman diagrams for bosons, and second, work by Natalie Jachowicz and co-workers [30], who developed a continous-time lattice Monte Carlo algorithm using the Hubbard-Stratonovich decomposition. The power of the new CT-QMC scheme is that it represents just the integration of the complex path integral without any transformation to effective non-interacting models and can be used for any complicated electron-electron vertex. We introduce the algorithm in the path integral formulation for the single-orbital Anderson impurity problem with a Hubbard-type interaction $U n_{\uparrow} n_{\downarrow}$. The generalization to the multiorbital case can be found in Ref. [20]. First, the action of the Anderson impurity model is divided

into a Gaussian part S_0 and an interaction part S_U as follows

$$S_0 = \sum_\sigma \int_0^\beta d\tau \int_0^\beta d\tau' c_\sigma^*(\tau)[(\partial_\tau - \mu + U\alpha_{-\sigma}(\tau))\delta(\tau - \tau') + \Delta(\tau - \tau')]c_\sigma(\tau') , \quad (41)$$

$$S_U = U \int_0^\beta d\tau [c_\uparrow^*(\tau)c_\uparrow(\tau) - \alpha_\uparrow(\tau)][c_\downarrow^*(\tau)c_\downarrow(\tau) - \alpha_\downarrow(\tau)] . \quad (42)$$

The parameters α are introduced to control the sign problem. A formal series expansion for the partition function is obtained by expanding the exponential in the interaction term,

$$\mathcal{Z} = \int \mathcal{D}[c^*, c]e^{-S_0[c^*,c]} \sum_{k=0}^\infty \frac{(-1)^k}{k!} U^k \int_0^\beta d\tau_1 \dots \int_0^\beta d\tau_k \, [c_\uparrow^*(\tau_1)c_\uparrow(\tau_1) - \alpha_\uparrow(\tau_1)]$$
$$[c_\downarrow^*(\tau_1)c_\downarrow(\tau_1) - \alpha_\downarrow(\tau_1)] \dots [c_\uparrow^*(\tau_k)c_\uparrow(\tau_k) - \alpha_\uparrow(\tau_k)][c_\downarrow^*(\tau_k)c_\downarrow(\tau_k) - \alpha_\downarrow(\tau_k)] . \quad (43)$$

Using the definition of the average over the noninteracting action

$$\langle \dots \rangle_0 = \frac{1}{\mathcal{Z}_0} \int \mathcal{D}[c^*, c] \dots \exp(-S_0), \quad (44)$$

the partition function can be expressed in the following form

$$\mathcal{Z} = \mathcal{Z}_0 \sum_{k=0}^\infty \int_0^\beta d\tau_1 \dots \int_{\tau_{k-1}}^\beta d\tau_k \, \mathrm{sgn}(\Omega_k) \, |\Omega_k| , \quad (45)$$

where the integrand is given by

$$\Omega_k = (-1)^k U^k \langle [c_\uparrow^*(\tau_1)c_\uparrow(\tau_1) - \alpha_\uparrow(\tau_1)][c_\downarrow^*(\tau_1)c_\downarrow(\tau_1) - \alpha_\downarrow(\tau_1)] \dots$$
$$\dots [c_\uparrow^*(\tau_k)c_\uparrow(\tau_k) - \alpha_\uparrow(\tau_k)][c_\downarrow^*(\tau_k)c_\downarrow(\tau_k) - \alpha_\downarrow(\tau_k)] \rangle_0 . \quad (46)$$

Note that here the range of time integration has been changed such that time ordering is explicit: $\tau_1 < \dots < \tau_{k-1} < \tau_k$. For a given set of times, all $k!$ permutations of this sequence contribute to Eq. (43). These can be brought into the standard sequence by permuting quadruples of Grassmann numbers, and hence without gaining an additional sign. Since all terms are subject to time-ordering, their contribution to the integral is identical, so that the factor $1/k!$ in Eq. (43) cancels. A configuration can be fully characterized by specifying a perturbation order k and a set of k times: $C_k = \{\tau_1, \dots, \tau_k\}$.

The Monte Carlo algorithm performs importance sampling over this configuration space. The weight of a configuration is thereby taken to be equal to the modulus of the integrand, Eq. (46). Since S_0 is Gaussian, the average over the noninteracting system can be evaluated using Wick's theorem. Hence, the weight of a configuration is essentially given by a fermionic determinant of a matrix containing the bare Green functions

$$\Omega_k = (-1)^k U^k \prod_\sigma \det \hat{g}^\sigma, \quad (47)$$
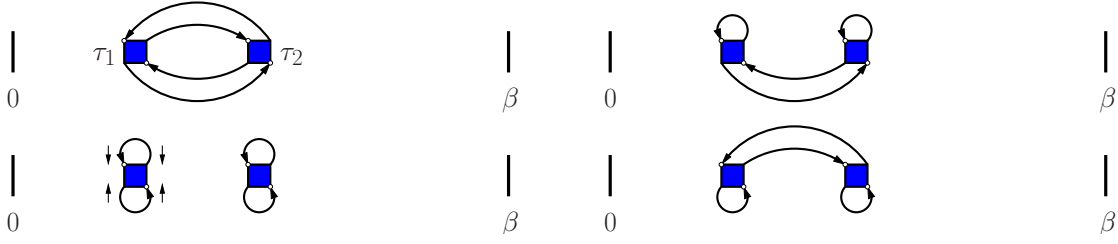
Fig. 8: *The four contributions to the partition function for $k = 2$. The interaction vertices are depicted by squares. Bare Green functions are shown as lines.*

where the local Green function in the α fields is equal to

$$(\hat{g}^\sigma)_{ij} = g_0^\sigma(\tau_i - \tau_j) - \alpha_\sigma(\tau_i)\delta_{ij} . \tag{48}$$

Note that determinants for different spin orientations factorize since the Green function is diagonal in spin-space.

The hybridization expansion (CT-HYB) or strong-coupling algorithm was initially introduced by Philipp Werner *et al.* [28] and has been generalized to multiorbital systems with general interactions [31, 32]. Here, the algorithm is discussed in the segment representation, which exploits the possibility of a very fast computation of the trace for a density-density type of interaction. The action is regrouped into the atomic part

$$S_{\text{at}} = \int_0^\beta d\tau \sum_\sigma c_\sigma^*(\tau)[\partial_\tau - \mu]c_\sigma(\tau) + U \int_0^\beta d\tau c_\uparrow^*(\tau)c_\uparrow(\tau)c_\downarrow^*(\tau)c_\downarrow(\tau) \tag{49}$$

and the part of the action S_Δ which contains the hybridization term:

$$S_\Delta = \int_0^\beta d\tau' \int_0^\beta d\tau \sum_\sigma c_\sigma^*(\tau)\Delta(\tau - \tau')c_\sigma(\tau') . \tag{50}$$

Here, the sign is taken out by reversing the original order of c and c^* to avoid an alternating sign in the expansion. To simplify the notation, consider first the spinless fermion model, which is obtained by disregarding the spin sums and interaction in Eqs. (49), (50). The series expansion for the partition function is generated by expanding in the hybridization term:

$$\begin{aligned}\mathcal{Z} = \; & \int \mathcal{D}[c^*, c]e^{-S_{\text{at}}} \sum_k \frac{1}{k!} \int_0^\beta d\tau_1' \int_0^\beta d\tau_1 \ldots \int_0^\beta d\tau_k' \int_0^\beta d\tau_k \times \\ & \times c(\tau_k)c^*(\tau_k')\ldots c(\tau_1)c^*(\tau_1')\Delta(\tau_1 - \tau_1')\ldots\Delta(\tau_k - \tau_k').\end{aligned} \tag{51}$$

The important observation now is that, at any order, the diagrams can be collected into a determinant of hybridization functions. The partition function then takes the form

$$\begin{aligned}\mathcal{Z} = \; & \mathcal{Z}_{\text{at}} \sum_k \int_0^\beta d\tau_1' \int_{\tau_1'}^\beta d\tau_1 \ldots \int_{\tau_{k-1}}^\beta d\tau_k' \int_{\tau_k'}^{\circ\tau_k} d\tau_k \times \\ & \times \langle c(\tau_k)c^*(\tau_k')\ldots c(\tau_1)c^*(\tau_1')\rangle_{\text{at}} \det \hat{\Delta}^{(k)},\end{aligned} \tag{52}$$

where the average is over the states of the atomic problem described by S_{at}. Here $\det \hat{\Delta}^{(k)}$ denotes the determinant of the matrix of hybridizations $\hat{\Delta}_{ij} = \Delta(\tau_i - \tau_j')$. The diagrams contributing to the partition function for $k = 3$ are shown in Fig. 9. A diagram is depicted by a
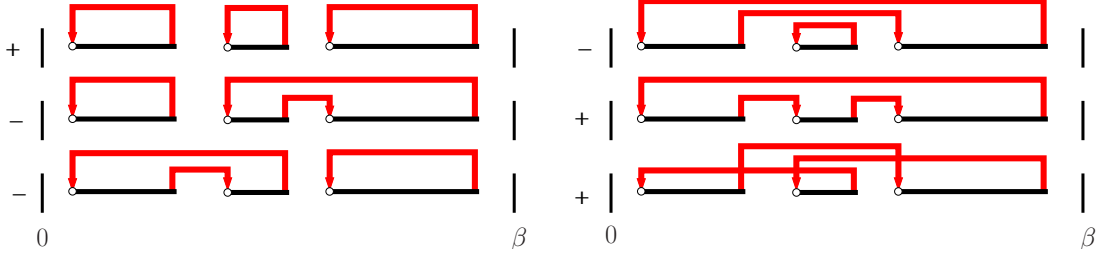
Fig. 9: *Diagrammatic representation of the six contributions to the partition function for spin-less fermions at $k = 3$. An electron is inserted at the start of a segment (marked by an open circle) and removed at the segment endpoint. The hybridization function lines $\Delta(\tau_i - \tau_j')$ (shown in red) are connected to the segments in all possible ways. The sign of each diagram is given on the left. Reproduced from Ref. [28].*
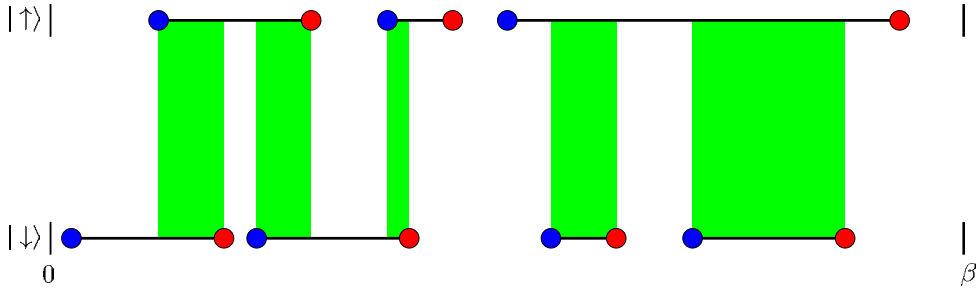

Fig. 10: *Example one band CT-HYB in a segment picture: The blue dots illustrate an annihi-lation operator, the red ones a creation operator and the black line represent the hybridization function $\Delta(\tau_i - \tau_j')$. The green region represents the time intervals at which two electrons are present on the impurity.*

collection of segments, where a segment is symbolic for the time interval where the impurity is occupied. The collection of diagrams obtained by connecting the hybridization lines in all possible ways corresponds to the determinant. Collecting the diagrams into a determinant is essential to alleviate or completely suppress the sign problem. Note that the imaginary time interval in Eq. (52) is viewed as a circle denoted by $\circ\tau_k'$. The trajectories in the path integral are subject to antiperiodic boundary conditions, which is accommodated by an additional sign if a segment winds around the circle.

For the single-orbital Anderson impurity model with Hubbard interaction, the segment picture still holds and gives a very intuitive picture of the imaginary time dynamics. A configuration is visualized by two separate timelines, one for each spin. The additional sum over spins, $\sum_{\sigma_1...\sigma_k}$, which enters in the first line of Eq. (52), generates contributions such as the one shown in Fig. 10. The only difference to the spinless fermion model is that when the impurity is doubly occupied the energy U has to be paid and the trace is $e^{\mu(l_\uparrow + l_\downarrow) - Ul_d}$, where l_σ is the time spent on the impurity for an electron with spin σ and l_d is the time the impurity is doubly occupied.

In Fig. 11, we shows comparison of the CT-INT and CT-HYB for the strong-coupling case $U \geq W$ of a single band model. The perfect agreement of these two complementary CT-QMC schemes supports the important statement about the possibility of a numerically exact solution of the quantum impurity problem.
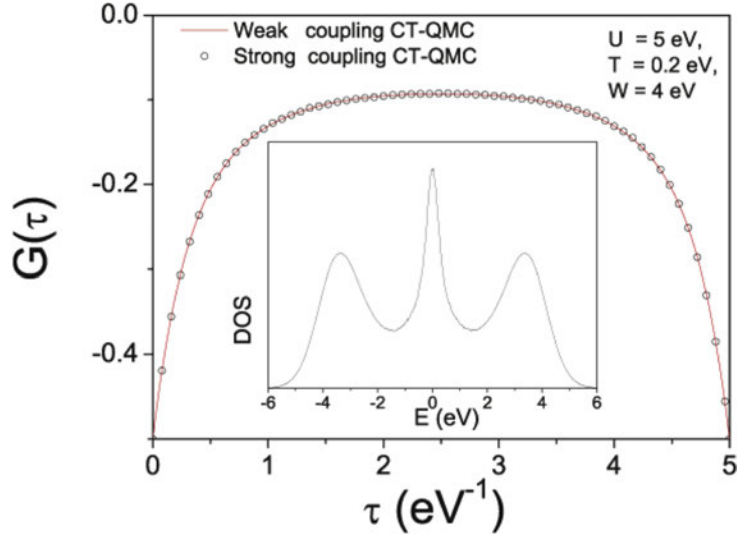
Fig. 11: *Comparisson of the weak coupling (CT-INT) and strong coupling (CT-HYB) CT-QMC impurity solvers for one-band semicircular model with $U \geq W$. In the insert, the density of states obtained with maximum entropy scheme is shown.*

5   LDA+DMFT scheme for real materials

In order to investigate real correlated systems with the local DMFT scheme, we need to have an efficient scheme of partitioning the space and orbital degrees of freedom. For example, in the high-temperature superconducting oxide $YBa_2Cu_3O_7$, the strongly correlated electrons are in the Cu $3d$ orbitals, and moreover there is only one per non-equivalent copper $d_{x^2-y^2}$ band that crosses the Fermi level with strong many-body fluctuations, i.e., just a few of the electronic states need to be included in the DMFT calculations. Therefore the simplest realistic correlated scheme would be a DFT+DMFT approach [33, 34] with partitioning of the orbital space into normal band electrons $|K\rangle$ described by the DFT Bloch basis and correlated local orbitals $|L\rangle$ described by some optimal Wannier basis (see Fig. 12 for an illustration).

The treatment of correlated electron systems requires the calculation of Green functions and hybridization functions in terms of local orbitals. This is readily achieved when using a basis set that is localized in real space, such as linear (or N-th order) muffin-tin orbitals (NMTO) [35] or Gaussian basis sets [37]. However, many implementations of density-functional theory use a delocalized plane wave basis set. This has the advantages that the basis set is simple and universal and that its convergence is controlled in principle by a single parameter, the energy cutoff. The projector augmented-wave method (PAW) [38], being representative of plane-wave-based methods, can be used as a simple example of the general projection scheme from the Bloch to the local basis: $\langle K|L\rangle$ (Fig. (12)).

Following the general projection scheme of Ref. [36,37], the desired quantity for the implementation of a DFT+DMFT method is a projection $\mathcal{P}^{\mathcal{C}} = \sum_L |L\rangle \langle L|$ of the full DFT Kohn-Sham Green function $G_{\mathrm{KS}}(\omega)$ on a set of localized orbitals $\{|L\rangle\}$

$$G^{\mathcal{C}}(\omega) = \mathcal{P}^{\mathcal{C}} G^{\mathrm{KS}}(\omega) \mathcal{P}^{\mathcal{C}}. \tag{53}$$
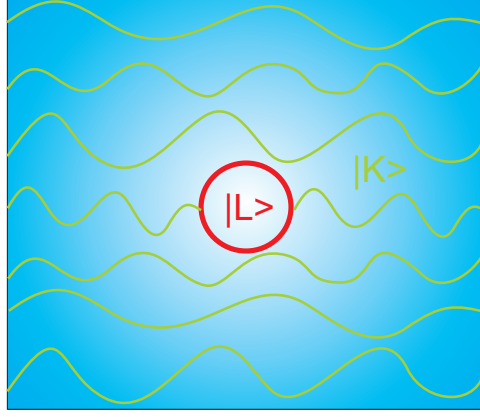
Fig. 12: *Schematic representation of the projection scheme from the Bloch basis to a local Wannier correlated subset.*

The subspace $\mathcal{C} = \mathrm{span}(\{|L\rangle\})$ is usually called the correlated subspace. It is the subspace of orbitals in which many-body fluctuations play a major role and where the DMFT corrections to the DFT will be considered. In plane-wave-based calculations, $G^{\mathrm{KS}}(\omega)$ in Matsubara space is available in terms of an almost complete set of Bloch states $|K\rangle$ that are eigenstates of the Kohn-Sham Hamiltonian $H_{\mathrm{KS}}|K\rangle = \varepsilon_K |K\rangle$

$$G_{\mathrm{KS}}(\omega) = \sum_K \frac{|K\rangle \langle K|}{i\omega + \mu - \varepsilon_K}. \tag{54}$$

Inserting equation (54) into equation (53) shows that one needs to evaluate projections of the type $\langle L|K\rangle$ in order to access the matrix elements $G^{\mathcal{C}}_{LL'}(\omega)$ of the local Green function. In most cases the correlated orbitals are d or f orbitals, which are localized inside the PAW augmentation spheres to a good approximation. For $|L\rangle$ within these spheres and given the PAW decomposition [38] of a Bloch state $|K\rangle$ one obtains

$$\langle L|K\rangle = \sum_i \langle L|\phi_i\rangle\langle \tilde{p}_i|\tilde{K}\rangle. \tag{55}$$

The index i of the augmentation functions $|\phi_i\rangle$ includes site s, angular momentum l and m as well as an index ν labeling the radial function: $i = (s, l, m, \nu)$, and $|\tilde{p}_i\rangle$ are the projectors of the PAW scheme.

In the described projection-scheme the $|L\rangle\langle L|$ matrix is not properly normalized for two reasons: (1) the Bloch basis is incomplete since only a limited number of Bloch bands is included and (2) the PAW augmentation functions are in general not orthonormal. The simplest way is to orthonormalize the projection matrices by the following Wannier-type construction: by definition, the localized states $|L\rangle$ are labeled by site and angular momentum indices: $L = (s, l, m)$. We split the site index $s = \mathbf{R} + \mathbf{T}$ such that $\mathbf{R}$ labels the position within the unit cell and $\mathbf{T}$ is the Bravais lattice vector of the unit cell in which s is located. This allows us to construct the Bloch transform of the localized states,

$$|L_{\mathbf{k}}\rangle = \sum_T e^{i\mathbf{k}\mathbf{T}} |L_{\mathbf{T}}\rangle, \tag{56}$$

where $\mathbf{k}$ is from the first Brillouin zone and $|L_{\mathbf{T}}\rangle \equiv |L\rangle = |s, l, m\rangle$. The sum in equation (56) runs over the Bravais lattice. Labeling the Bloch states $|K\rangle = |\mathbf{k}, n\rangle$ by their crystal momentum, $\mathbf{k}$, and band index, n, we normalize our projection matrices $\mathcal{P}_{Ln}^{\mathcal{C}}(\mathbf{k}) = \langle L_{\mathbf{k}} | \mathbf{k}, n \rangle$ using the overlap operator

$$O_{LL'}(\mathbf{k}) = \sum_n \mathcal{P}_{Ln}^{\mathcal{C}}(\mathbf{k}) \mathcal{P}_{L'n}^{*\mathcal{C}}(\mathbf{k}) \tag{57}$$

in

$$\bar{\mathcal{P}}_{Ln}^{\mathcal{C}}(\mathbf{k}) = \sum_{L'} O_{LL'}^{-1/2}(\mathbf{k}) P_{L'n}^{\mathcal{C}}(\mathbf{k}). \tag{58}$$

These orthonormalized projection matrices are calculated once at the beginning of any calculation and can then be used to obtain the local Green function of the correlated orbitals from the full Bloch Green function $G_{nn'}^{B}$

$$G_{LL'}^{\mathcal{C}}(\omega) = \sum_{\mathbf{k}, nn'} \bar{\mathcal{P}}_{Ln}^{\mathcal{C}}(\mathbf{k}) G_{nn'}^{B}(\mathbf{k}, \omega) \bar{\mathcal{P}}_{L'n'}^{*\mathcal{C}}(\mathbf{k}).$$

Similarly the hybridization function, $\Delta(\omega)$, is available. It is related to the local Green function by

$$G^{-1}(\omega) = i\omega - \epsilon_d - \Delta(\omega), \tag{59}$$

where ϵ_d is the static crystal field. Equation (59) is a matrix equation with G, Δ, and ϵ_d being $(\dim \mathcal{C}) \times (\dim \mathcal{C})$ matrices, in general. To separate the hybridization from the static DFT crystal field, we numerically evaluate the limit $\omega \to \infty$, where $\omega - G^{-1}(\omega) \to \epsilon_d$.

In a DFT+DMFT calculation the projection matrices $\bar{\mathcal{P}}_{Ln}^{\mathcal{C}}(\mathbf{k})$ are used for up- and downfolding quantities like the Green function and the self-energy in the course of the iterative DMFT procedure in exactly the same way as shown for the local Green function above. For example, the self energy obtained by an impurity solver for the effective impurity model $\Sigma_{LL'}^{\mathcal{C}}(\omega)$ can be upfolded to the Bloch basis as follows:

$$\Sigma_{nn'}^{B}(\mathbf{k}, \omega) = \sum_{LL'} \overline{P}_{Ln}^{*\mathcal{C}}(\mathbf{k}) \, \Sigma_{LL'}^{\mathcal{C}}(\omega) \, \overline{P}_{L'n'}^{\mathcal{C}}(\mathbf{k}).$$

Since the self energy in DMFT is a purely local quantity, the index $\mathbf{k}$ on $\Sigma_{nn'}^{B}(\mathbf{k}, \omega)$ reflects the momentum dependence brought about by the projection matrices. The presented projection scheme allows for the inclusion of both correlated and uncorrelated states in the procedure. Therefore, information about the interplay of correlated orbitals with their uncorrelated ligands can be obtained.

Figure 13 shows that the DFT+DMFT calculation commences with the solution of the Kohn-Sham equations by DFT. In a second step the projection onto the correlated subset is computed. The Kohn-Sham Green function is then computed and used as an initial guess for the mean-field $\mathcal{G}$ of the DMFT cycle, which consists of the usual steps detailed before. In usual applications the DFT+DMFT loop will stop after DMFT self-consistency is obtained. It has, however, recently become possible to continue the cycle supplying the DFT code with an altered charge density that includes correlation effects. In such a unified approach changes in the charge density
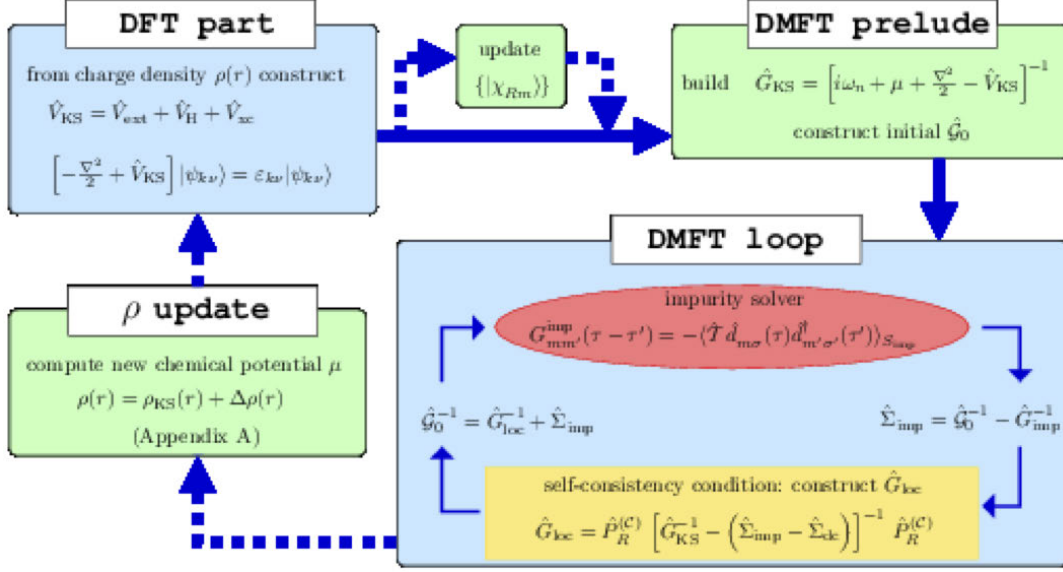
Fig. 13: *Illustration of the DFT+DMFT procedure. As a first step, the Kohn-Sham (KS) equations, determining the Kohn-Sham potential and thus the Hamiltonian, are solved. Secondly, the KS Green function and from it the starting value for the bath Green function $\mathcal{G}$ is constructed and passed on to the DMFT loop, which consists of the usual steps described before. A potential self-consistency over the charge density is also indicated [37].*

induced by correlations can be studied [37, 40]. It allows furthermore for the accurate calculation of total energies, which allow the determination of crystal structures and other coupled electronic and structural effects.

As example, we show a realistic DFT+DMFT calculation of the $SrVO_3$ spectral function in the Fig.14, where one can see the renormalisation of the valence correlated V t_{2g} states as well as broadening of the Bloch O $2p$ states [39].

6 Problem of double counting

We will finally discuss the problem of double-counting corrections in the LDA+DMFT scheme [41]. We use the standard definitions of the parameters U and J

$$U = F^0 \quad \text{and} \quad J = \frac{F^2 + F^4}{14}. \tag{60}$$

Over the years different methods to fix μ_{DC} have been devised. Two main approaches are the around mean-field (AMF) approximation and the fully localized or atomic limit (FLL) [7]. Both methods use analytic arguments to devise a double counting correction. The AMF is based on the conjecture that DFT corresponds to a mean-field solution of the many-body problem. The resulting double counting potential can be written as

$$\mu_{DC}^{AMF} = U(N_{imp} - \bar{n}) - J(N_{imp}^\sigma - \bar{n}), \tag{61}$$

where N_{imp} is the total occupancy of the impurity, N_{imp}^σ the occupancy per spin ($N_{imp}^\sigma = N_{imp}/2$ for the paramagnetic case), and $\bar{n} = \frac{1}{2(2l+1)} \sum_{m,\sigma} n_{m\sigma}$ is the average occupancy. The AMF
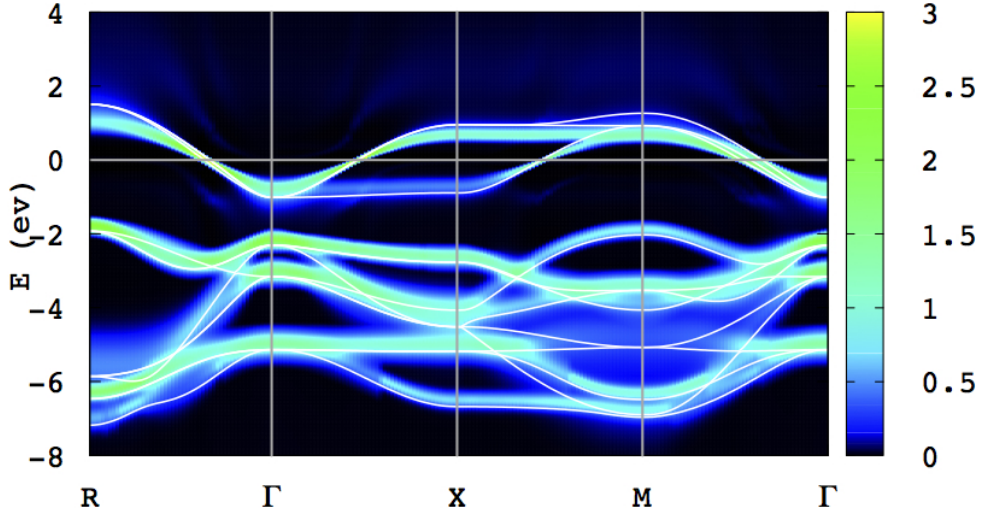
Fig. 14: *Momentum resolved impurity spectral function of SrVO$_3$ obtained by DFT+DMFT. The LDA band structure of the V t_{2g} and O $2p$ Bloch states is shown for comparison.*

functional is known to produce unsatisfactory results for strongly correlated systems, which led to the development of another method, the so-called FLL. The FLL functional takes the converse approach to the AMF and begins with the atomic limit. It has been shown that this new potential can also be written as a correction to the AMF solution [7], Eq. (61),

$$\mu_{\text{DC}}^{\text{FLL}} = U\left(N_{\text{imp}} - \frac{1}{2}\right) - J\left(N_{\text{imp}}^{\sigma} - \frac{1}{2}\right) = \mu_{\text{DC}}^{\text{AMF}} + (U - J)\left(\bar{n} - \frac{1}{2}\right).$$

This addition to the AMF potential has the effect of a shift of the centroid of the level depending on its occupation. An empty level is raised in energy by $\frac{1}{2}(U - J)$ and the converse happens to a fully occupied level. The form of the functional is based on the property of the *exact* density-functional that the one electron potential should jump discontinuously at integer electron number [7], a property which is not fulfilled in LDA or GGA. Ultimately the FLL leads to a stronger trend towards integer occupancies and localization. The general problem with analytic expressions like the ones presented above is that their scope is limited to certain classes of systems that fulfill the assumptions made in the derivation process. As an additional complication, both approaches can be used employing the average orbital occupancies obtained from DFT or in a self-consistent manner allowing the occupancies to be determined within the DFT+DMFT loop.

The obvious problems with analytical formulae make conceptually different approaches worth exploring. It would certainly be an improvement if the double counting could be found self-consistently along with the chemical potential in the DMFT self-consistency loop. One possible ansatz using the impurity self-energy $\Sigma_{mm'}^{\text{imp}}$ is to constrain the high energy tails in the real part of the self-energy to sum up to zero

$$\text{Re}[\text{Tr}(\Sigma_{mm'}^{\text{imp}}(i\omega_N))] = 0. \tag{62}$$

Here, ω_N is the highest Matsubara frequency included in the calculation. Physically this amounts to the requirement that the shift in the centroid of the impurity orbitals contains no static com-

ponent. Since the self-energy is a quantity computed self-consistently via the quantum Monte Carlo in our case, one has to ensure that a reasonably high number of Matsubara frequencies is included in the calculation and additionally that the Monte Carlo data is well converged. Double-counting corrections based on the self-energy have been applied successfully to metallic systems [42].

Another possible approach is to constrain the total charge in the impurity based on the Friedel sum rule [12]. The Friedel sum rule gives a zero-temperature relationship between the extra states induced below the Fermi level by a scattering center (an impurity) and the phase shift at the chemical potential. For the Anderson model the extra states induced are given by the occupation number of the impurity states, and the scattering potential is the hybridization that affects the conduction electrons. The simplest version requires the charges in the self-consistent bath and the impurity to be equal

$$\mathrm{Tr}\, G^{\mathrm{imp}}_{mm'}(\beta) \overset{!}{=} \mathrm{Tr}\, \mathcal{G}_{mm'}(\beta). \tag{63}$$

The value of the imaginary time Green function at $\tau = \beta$ gives the orbital occupancy, thus the trace over them amounts to the total occupancy of the impurity. Both versions of the method give very similar results and work well in metallic systems, since in a metal the total particle number of the system N_{tot} and of the impurity N_{imp} are both very sensitive to small variations in μ and μ_{DC}. Also the likeness to the Friedel sum rule, which applies to metals, indicates that such a constraint will work for metals only. As NiO has a quite large gap, the charge is almost invariant with respect to the chemical and the double-counting potential in the gap. Over a region of several electron volts
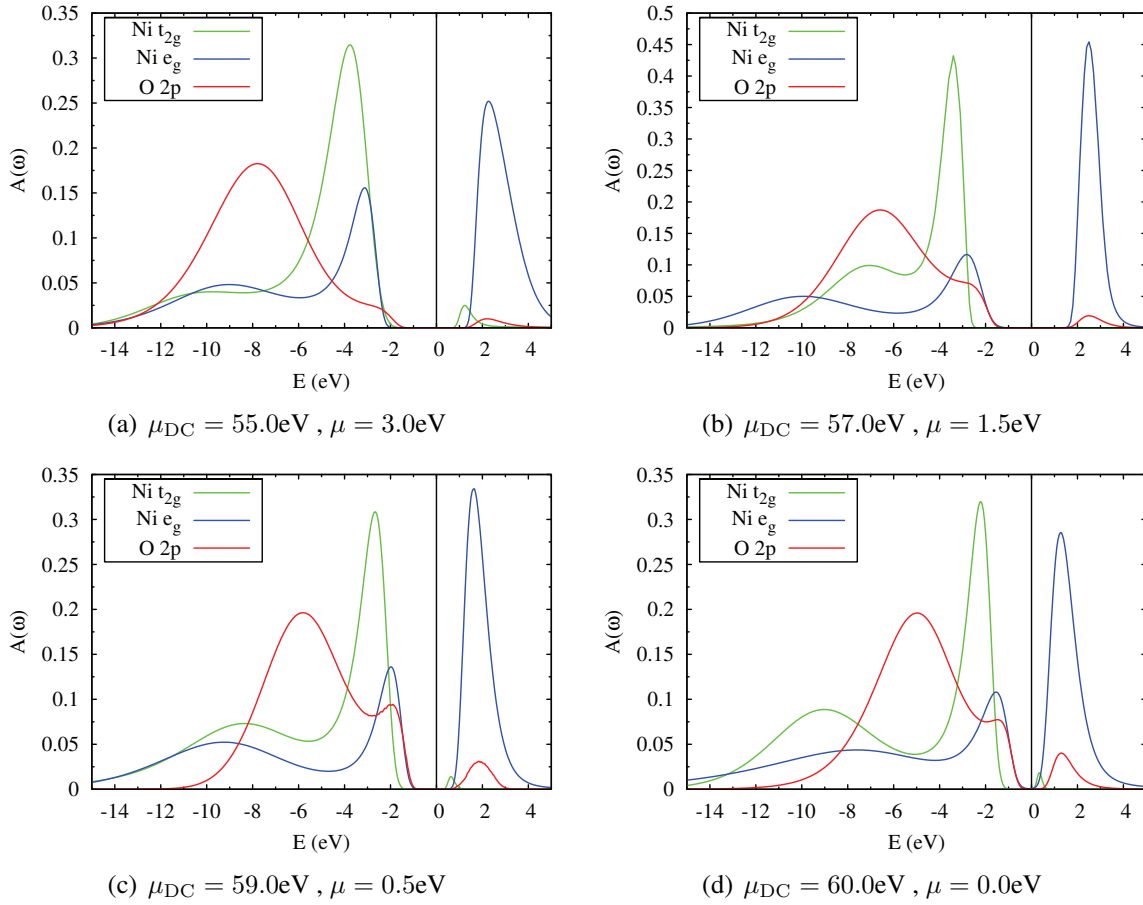
$$\frac{\delta N_{\mathrm{tot}}}{\delta \mu} \approx 0.$$

We will see below the consequences for this specific double-counting prescription and for double-countings in general that arise from the presence of the insulating gap.

Now that we have introduced the double-counting in the context of DFT+DMFT and discussed ways to fix the underlying parameter, we can elucidate our test case: NiO. The double-counting potential has been treated here as an adjustable parameter and has been varied between 55 eV and 60 eV. The most prominent effects of the double counting on the spectral properties are the shift of the oxygen $2p$ bands with respect to the nickel $3d$ bands, as well as the variation in gap size. The μ_{DC} controls the filling of the Ni $3d$ orbitals and since the total number of particles in the system is fixed at $N_{\mathrm{tot}} = 14$, the chemical potential μ of the full system must be varied together with μ_{DC}. The filling of the Ni $3d$ orbitals can be varied from $N_{\mathrm{imp}} \approx 8.1$ at $\mu_{\mathrm{DC}} = 55$ eV to $N_{\mathrm{imp}} \approx 8.3$ at $\mu_{\mathrm{DC}} = 60$ eV. The double counting potential μ_{DC} has profound impact on the spectrum $A_m(\omega) = -\frac{1}{\pi} G_m(\omega)$ shown in Fig. 15 and the k-resolved spectral function

$$A_m(\mathbf{k}, \omega) = -\frac{1}{\pi}\mathrm{Im}\left(\omega + \mu - \varepsilon_m(\mathbf{k}) - \Sigma^{\mathrm{imp}}_m(\mathbf{k}, \omega)\right)^{-1}$$
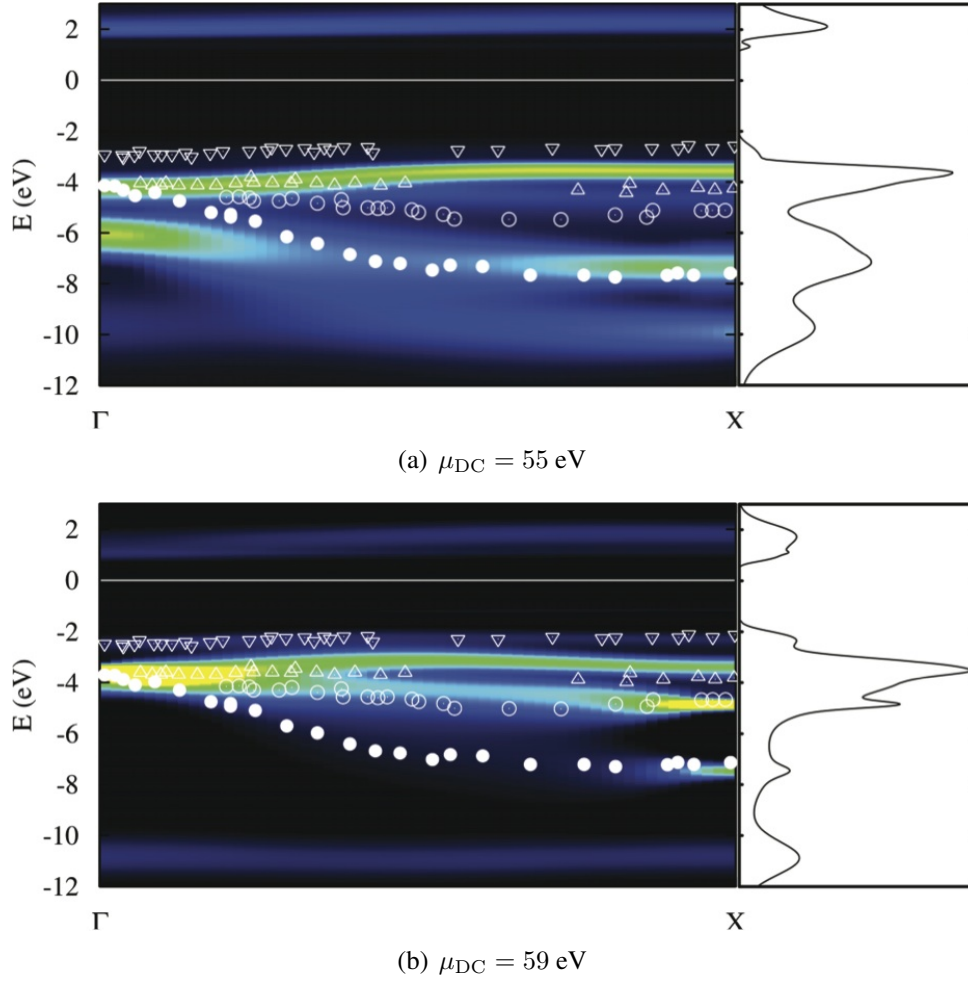
shown along the line $\Gamma - X$ in the Brillouin zone in Fig. 16. All spectral functions were obtained by the maximum entropy method from imaginary-time Green functions. With increasing μ_{DC},

(a) $\mu_{\mathrm{DC}} = 55.0\mathrm{eV}$, $\mu = 3.0\mathrm{eV}$

(b) $\mu_{\mathrm{DC}} = 57.0\mathrm{eV}$, $\mu = 1.5\mathrm{eV}$

(c) $\mu_{\mathrm{DC}} = 59.0\mathrm{eV}$, $\mu = 0.5\mathrm{eV}$

(d) $\mu_{\mathrm{DC}} = 60.0\mathrm{eV}$, $\mu = 0.0\mathrm{eV}$

Fig. 15: *LDA+DMFT spectral functions at $\beta = 5\mathrm{eV}^{-1}$ for different values of the double counting correction μ_{DC}, illustrating its impact on the spectrum [41].*

the system evolves from a large gap Mott insulator at $\mu_{\mathrm{DC}} = 55$ eV (Fig. 15 (a)), with a gap of about 4 eV opening between the Ni $3d$ states and almost no oxygen at the valence band edge, towards an almost closed-gap at $\mu_{\mathrm{DC}} = 60$ eV (Fig. 15 (d)). Plainly speaking, the double-counting correction allows for a tuning of the spectral properties from a large-gap Mott insulator in the region $\mu_{\mathrm{DC}} \leq 55$ eV to a metal at $\mu_{\mathrm{DC}} > 60$ eV. The regime of the charge transfer insulator, the expected physical state of NiO, lies somewhere in between at $\mu_{\mathrm{DC}} \sim 59$ eV (Fig. 15 (c)). In this state the oxygen states make up about half the spectral weight at the valence band edge, as observed in experiments [43, 44]. The gap, however, is much smaller than 4 eV, thus if the only criterion of the quality of the calculation would be the gap, the double-counting of choice would be around $\mu_{\mathrm{DC}} = 55$ eV, missing the physics of the system entirely.

Let us now turn to the **k**-resolved spectral functions shown in Fig. 16 and compare them with ARPES data [45]. We have superimposed the ARPES data on top of our calculated spectral functions; the data were aligned at the valence band edge to facilitate comparison. The uppermost band in Figs. 16 (a) and (b) at 2eV above the Fermi level is a Ni e_g band, while the other bands can be identified with the ones obtained by ARPES. The two lowest lying bands

(a) $\mu_{\mathrm{DC}} = 55$ eV

(b) $\mu_{\mathrm{DC}} = 59$ eV

Fig. 16: **k**-*resolved spectral functions $A(\mathbf{k}, \omega)$ along the line $\Gamma - X$ in the Brillouin zone for different values of the double counting μ_{DC}. On the right the spectra integrated along the shown crystal momentum direction are shown [41] .*

correspond to oxygen $2p$ states, the bands above are formed by Ni $3d$ states. The characteristic features seen in ARPES, like the broadening of the oxygen bands around the midpoint of the $\Gamma - X$ line, are clearly present. The quantitative features, especially the relative band energies can strongly differ, depending on the double counting chosen. The bands in Fig. 16 (a) ($\mu_{\mathrm{DC}} = 55$ eV) show a clear separation between the oxygen and the nickel part at the Γ-point as well as the X-point. At the increased value $\mu_{\mathrm{DC}} = 59$ eV, Fig. 16 (b), the oxygen bands are shifted towards the Fermi level, coming to overlap with the Ni $3d$ bands at the Γ-point as in the ARPES data. A detailed comparison of the calculated band structures with experiments shows that the bands calculated with $\mu_{\mathrm{DC}} = 59$ eV agree very well with the experimental data. These calculations reproduce the flat bands at -4 eV, and another at about -2 eV becomes more prominently visible at $\mu_{\mathrm{DC}} = 59$ eV, while it is very faint at $\mu_{\mathrm{DC}} = 55$ eV. The dispersive bands in the region -4 eV to -8 eV also agree very well with experiment. Calculations with other values of the double counting can strongly differ from the experimental data, as shown by the example of $\mu_{\mathrm{DC}} = 55$ eV.
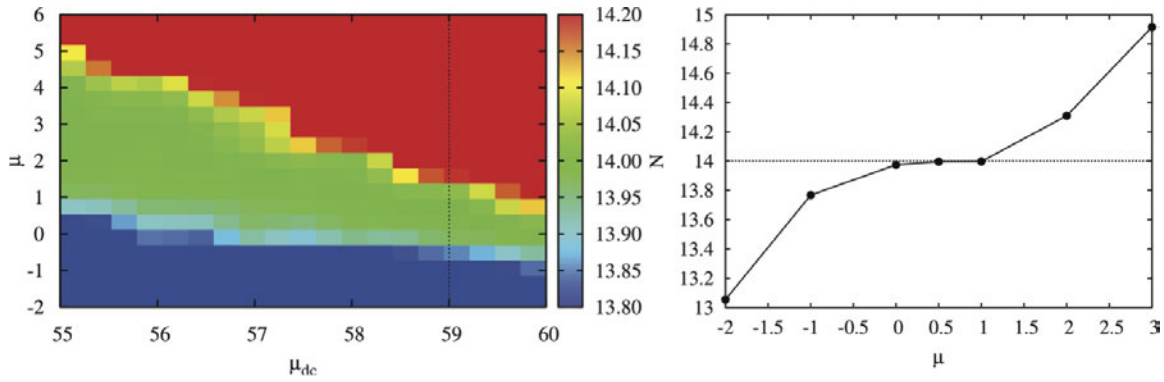
Fig. 17: *Surface created by different combinations of the chemical potential μ and the double counting potential μ_{DC}. The particle number has been color coded: the green plateau corresponds to a particle number very close to the desired value of 14, values below are encoded in blue, values above in red. In addition the dotted line indicates the location of the N vs μ curve for $\mu_{\mathrm{DC}} = 59$ eV that is shown on the right. The line is a guide to the eye only [41].*

The dimension of the double-counting problem becomes apparent when the parameter space of the overall chemical potential μ and the double counting potential μ_{DC} versus the total particle number in the system N is examined. The result is shown in Fig. 17 on the left with the particle number color coded. The picture shows that in principle any combination of μ and μ_{DC} that yields a point in the green plateau, corresponding to the desired particle number $N \approx 14$ *a priori* describes the system equivalently well.

7   Conclusions

We have learnt how to treat electronic correlations in correlated materials within the local DMFT scheme. This knowledge can be used in realistic LDA+DMFT calculations for strongly correlated transition-metals and rare-earth systems, where spin, orbital, and charge fluctuations in the d- or f-shell play a crucial role in photoemission spectra and in magnetic and optical excitations. The numerically exact solution of the quantum impurity problem gives us an effective local exchange-correlation functional for given correlated materials in a specific external field. The combination of DMFT with first-principles approaches is a very useful tool for the investigation of correlated electronic materials.

Acknowledgment

References

[1] P. Hohenberg and W. Kohn, Phys. Rev. **136**, B864 (1964)

[2] W. Kohn and L.J. Sham, Phys. Rev. **140**, A1133 (1965)

[3] D.M. Ceperley and B.J. Alder, Phys. Rev. Lett. **45**, 566 (1980)

[4] G. Ortiz and P. Ballone, Phys. Rev. B **50**, 1391 (1994)

[5] E.K.U. Gross and W. Kohn, Adv. Quantum Chem. **21**, 255 (1990)

[6] R.O. Jones and O. Gunnarsson, Rev. Mod. Phys. **61**, 689 (1989)

[7] V.I. Anisimov, F. Aryasetiawan, and A.I. Lichtenstein,
     J. Phys.: Condens. Matter **9**, 767 (1997)

[8] A. Damascelli, Z. Hussain, and Z.-X. Shen, Rev. Mod. Phys. **75**, 473 (2003)
     G. Kotliar and D. Vollhardt, Physics Today **57**, 53 (2004)

[9] L. de Medici, J. Mravlje, and A. Georges, Phys. Rev. Lett. **107**, 256401 (2011)

[10] G. Kotliar, S.Y. Savrasov, K. Haule, V.S. Oudovenko, O. Parcollet, and C.A. Marianetti,
     Rev. Mod. Phys. **78**, 865 (2006)

[11] A.B. Migdal: *Theory of finite Fermi Systems and applications to atomic nuclei*
     (Interscience Publishers, New York, 1967)

[12] P. Nozières: *Theory of interacting Fermi systems* (Benjamin, New York, 1964).

[13] G. Baym and L.P. Kadanoff, Phys. Rev. **124**, 287 (1961)

[14] M. Potthoff, Eur. Phys. J. B **32**, 429 (2003)

[15] R. van Leeuwen, N.E. Dahlen, and A. Stan, Phys. Rev. B **74**, 195105 (2006)

[16] A.N. Rubtsov, M.I. Katsnelson, and A.I. Lichtenstein, Phys. Rev. B **77**, 033101 (2008)

[17] H. Hafermann, F. Lechermann, A.N. Rubtsov, M.I. Katsnelson, A. Georges, and
     A.I. Lichtenstein, Lecture Notes in Physics **843**, 145 (2012)

[18] H. Hafermann, S. Brener, A.N. Rubtsov, M.I. Katsnelson, A.I. Lichtenstein,
     JETP Lett. **86**, 677 (2007)

[19] A.N. Rubtsov, M.I. Katsnelson, and A.I. Lichtenstein, Annals Phys. **327**, 1320 (2012)

[20] E. Gull, A.J. Millis, A.I. Lichtenstein, A.N. Rubtsov, M. Troyer, and P. Werner,
     Rev. Mod. Phys. **83**, 349 (2011)

[21] H. Hafermann, G. Li, A.N. Rubtsov, M.I. Katsnelson, A.I. Lichtenstein, and H. Monien, Phys. Rev. Lett. **102**, 206401 (2009)

[22] A. Georges, G. Kotliar, W. Krauth, and M.J. Rozenberg, Rev. Mod. Phys. **68** , 13 (1996)

[23] W. Metzner and D. Vollhardt, Phys. Rev. Lett. **62**, 324 (1989)

[24] E. Pavarini, E. Koch, and A.I. Lichtenstein, Phys. Rev. Lett. **101**, 266405 (2008)

[25] A.N. Rubtsov, M.I. Katsnelson, A.I. Lichtenstein, and A. Georges, Phys. Rev. B **79**, 045133 (2009)

[26] A.A. Abrikosov, L.P. Gorkov, and I.E. Dzyaloshinskii: *Methods of Quantum Field Theory in Statistical Physics* (Pergamon Press, New York, 1965)

[27] A.N. Rubtsov and A.I. Lichtenstein, JETP Lett. **80**, 61 (2004)

[28] P. Werner, A. Comanac, L. de Medici, M. Troyer, and A.J. Millis, Phys. Rev. Lett. **97**, 076405 (2006)

[29] N.V. Prokofev, B.V. Svistunov, and I.S. Tupitsyn, JETP Sov. Phys. **87**, 310 (1998)

[30] S.M.A. Rombouts, K. Heyde, and N. Jachowicz, Phys. Rev. Lett. **82**, 4155 (1999)

[31] P. Werner and A.J. Millis, Phys. Rev. B **74**, 155107 (2006)

[32] K. Haule, Phys. Rev. B **75**, 155113 (2007)

[33] V.I. Anisimov, A.I. Poteryaev, M.A. Korotin, A.O. Anokhin, and G. Kotliar, J. Phys.: Condensed Matter **9**, 7359 (1997)

[34] A.I. Lichtenstein and M.I. Katsnelson, Phys. Rev. B **57**, 6884 (1998)

[35] O.K. Andersen and T. Saha-Dasgupta, Phys. Rev. B **62**, R16219 (2000)

[36] V.I. Anisimov, D.E. Kondakov, A.V. Kozhevnikov, I.A. Nekrasov, Z.V. Pchelkina, J.W. Allen, S.-K. Mo, H.-D. Kim, P. Metcalf, S. Suga, A. Sekiyama, G. Keller, I. Leonov, X. Ren and D. Vollhardt, Phys. Rev. B **71**, 125119 (2005)

[37] F. Lechermann, A. Georges, A. Poteryaev, S. Biermann, M. Posternak, A. Yamasaki and O.K. Andersen, Phys. Rev. B **74**, 125120 (2005)

[38] P.E. Blöchl, Phys. Rev. B **50**, 17953 (1994)

[39] M. Karolak, T.O. Wehling, F. Lechermann and A.I. Lichtenstein, J. Phys.: Condens. Matter **23**, 085601 (2011)

[40] D. Grieger, C. Piefke, O.E. Peil, and F. Lechermann, Phys. Rev. B **86**, 155121 (2012)

[41] M. Karolak, G. Ulm, T. Wehling, V. Mazurenko, A. Poteryaev, and A. Lichtenstein, J. Electr. Spectr. **181**, 11 (2010)

[42] A.I. Lichtenstein, M.I. Katsnelson, and G. Kotliar, Phys. Rev. Lett. **87**, 067205 (2001).

[43] G.A. Sawatzky and J.W. Allen, Phys. Rev. Lett. **53**, 2339 (1984)

[44] D.E. Eastman and J.L. Freeouf, Phys. Rev. Lett. **34**, 395 (1975)

[45] Z.X. Shen, C.K. Shih, O. Jepsen, W.E. Spicer, I. Lindau, and J.W. Allen, Phys. Rev. Lett. **64**, 2442 (1990)